Jurnal Polimesin
Department of Mechanical Engineering
State Polytechnic of Lhokseumawe
http://e-jurnal.pnl.ac.id/polimesin
e-ISSN : 2549-1999 No. : 3 Month : June
p-ISSN : 1693-5462 Volume : 24 Year : 2026

Processing dates: received on 2026-5-11, reviewed on 2026-05-23, accepted on 2026-06-04 and online availability on 2026-06-30

CFD-based thermal limit prediction of $LiFePO_4$ submarine battery modules using UDF heat generation and hybrid cooling

Fajri Narotama, Prabowo*
Department of Mechanical Engineering, Sepuluh Nopember Institute of Technology, Surabaya 60111, Indonesia
*Corresponding Author: prabowo@me.its.ac.id

Abstract

This study investigates the transient thermal behavior of $LiFePO_4$ battery modules in a diesel-electric submarine battery compartment under constant 1C and 1.4C discharge conditions. A three-dimensional CFD model was developed in ANSYS® Fluent, with conjugate heat transfer between the battery modules, the air domain, and the liquid cooling channels. Battery heat generation was calculated through a compiled User-Defined Function derived from an equivalent-circuit heat-generation formulation. The module was represented as a homogenized orthotropic solid, allowing the compartment-scale model to be solved without resolving each cell. The heat-source model was validated against published experimental data for a 100 Ah prismatic LFP cell, yielding an RMSE of 0.28°C and an MAE of 0.24°C. At 1C discharge, hybrid cooling reduced the final maximum temperature from 48.25 °C to 45.26°C, while both cooling configurations remained below the 50°C thermal cutoff. At 1.4C discharge, natural convection reached the cutoff at 2140 s, whereas hybrid cooling delayed it to 2403 s, extending the operating window by 263 s (12.3%). Although the reduction in final maximum temperature was limited, the average temperature decreased by 5.62°C. These results indicate that hybrid cooling mainly reduces global heat accumulation, while internal heat conduction remains the dominant factor governing local hotspot formation.

Keywords:
$LiFePO_4$ submarine battery, CFD thermal management, UDF heat generation, equivalent circuit model, orthotropic homogenization, hybrid cooling, thermal cutoff time.

1 Introduction

Lithium iron phosphate ($LiFePO_4$ or LFP) batteries are being considered for diesel-electric submarines and electric-powered vessels because they can improve underwater endurance and propulsion efficiency [6][14]. For submarine use, $LiFePO_4$ is attractive because it is generally more thermally stable and has a longer cycle life than lead-acid batteries and several high-energy cobalt-based lithium-ion chemistries [6][7]. This behavior is commonly associated with the phosphate-based cathode structure, although the energy density of LFP is still lower than that of several high-energy lithium-ion chemistries [1][7]. The stability advantage does not mean that cooling can be ignored. During high C-rate operation, the battery can still generate substantial heat and develop a non-uniform temperature field, so a thermal management system is still required [1][2].

The cooling challenge is more severe in a submarine battery room, where many modules are placed in a confined compartment with limited space for heat removal [9][15]. During high-load submerged operation, the battery modules generate heat from ohmic and polarization losses and reversible entropic effects [3][4][13]. If this heat is not removed effectively, localized hotspots and non-uniform temperature fields may develop, accelerating degradation and increasing the possibility of protection-triggered operational interruption [11][16][17]. In submarine applications, this risk is more important because the battery space is located close to other mission-critical components, including fuel tanks and torpedo storage areas.

Battery thermal management has been widely studied for electric vehicles, single cells, small packs, cold plates, air cooling, liquid cooling, and hybrid cooling arrangements [3][5][7][18][19]. Those studies are useful as a basis for battery-cooling analysis, but the layout of a submarine battery room imposes several restrictions. The air path is shorter and more confined, the heat rejection route is limited, and the modules are arranged in a dense tier rather than an open-pack configuration [6][9][15][20]. Work that directly addresses compartment-scale thermal management of $LiFePO_4$ submarine battery modules is still limited. Existing submarine battery studies more often discuss battery management, charging systems, and operational reliability than CFD-based thermal prediction in a confined battery compartment [21]. Maritime battery studies also note that shipboard battery spaces must account for thermal runaway, fire, explosion, toxic gas, water ingress, and coolant leakage risks [22]. In addition, maritime electrification studies connect onboard batteries with power system integration and vessel operating profiles [23]. For this reason, the present study focuses on transient compartment-scale thermal prediction for a $LiFePO_4$ submarine battery module, with the cutoff time treated as part of the operational safety assessment.

Several recent CFD and system-level BTMS studies point to the same issue: cooling performance depends not only on cooling capacity but also on how air is distributed, where cooled boundaries are placed, and how uniform the temperature field remains in a dense battery arrangement [24][25]. Electrochemical-thermal studies also report that higher discharge rates increase heat generation and tend to make the temperature field less uniform, especially in large-format lithium-ion cells [11][14][26]. Liquid-channel and cold-plate studies further show that boundary cooling can reduce the average temperature, while the hottest point may still be limited by the internal conduction path within the cell or module [15][17][27]. In the present work, these findings are applied to a confined submarine battery compartment, and the time required to reach the protection threshold is treated as both a thermal-performance result and an operational safety indicator.

The objective of this study is to predict the transient thermal limit of a $LiFePO_4$ submarine battery module under compartment-scale cooling conditions using a CFD model with UDF-based heat generation (Fig. 1). Specifically, this study aims to: (1) validate the electro-thermal heat-source formulation using published 100 Ah prismatic LFP cell data [3]; (2) compare natural convection and hybrid cooling under constant 1C and 1.4C discharge conditions; (3) evaluate T_{max}, T_{avg}, and the time required to reach the 50 °C thermal cutoff limit; and (4) identify whether hybrid cooling mainly reduces local hotspots or global heat accumulation in the battery module.

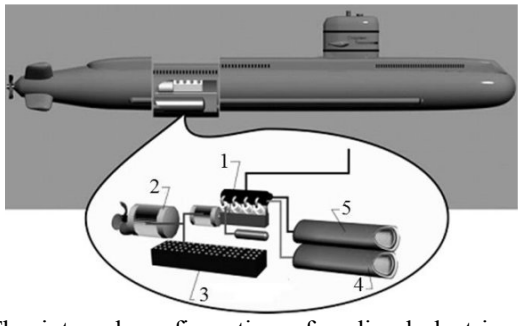

Fig. 1. The internal configuration of a diesel-electric submarine demonstrates the placement of the large-scale lithium-ion battery module (Component 3) within the restricted compartment [14]

2 Research methodology

2.1 Geometry model

The computational domain represents a diesel-electric submarine battery compartment containing a full-tier LFP battery assembly. The model was constructed to capture heat transfer between the battery solid structures and the surrounding fluid regions [6][8]. The battery assembly consists of 600 LFP cells arranged in a 15-series and 40-parallel configuration (Fig. 2). Each cell has a nominal capacity of 100 Ah and a nominal voltage of 3.2 VDC [3][5].

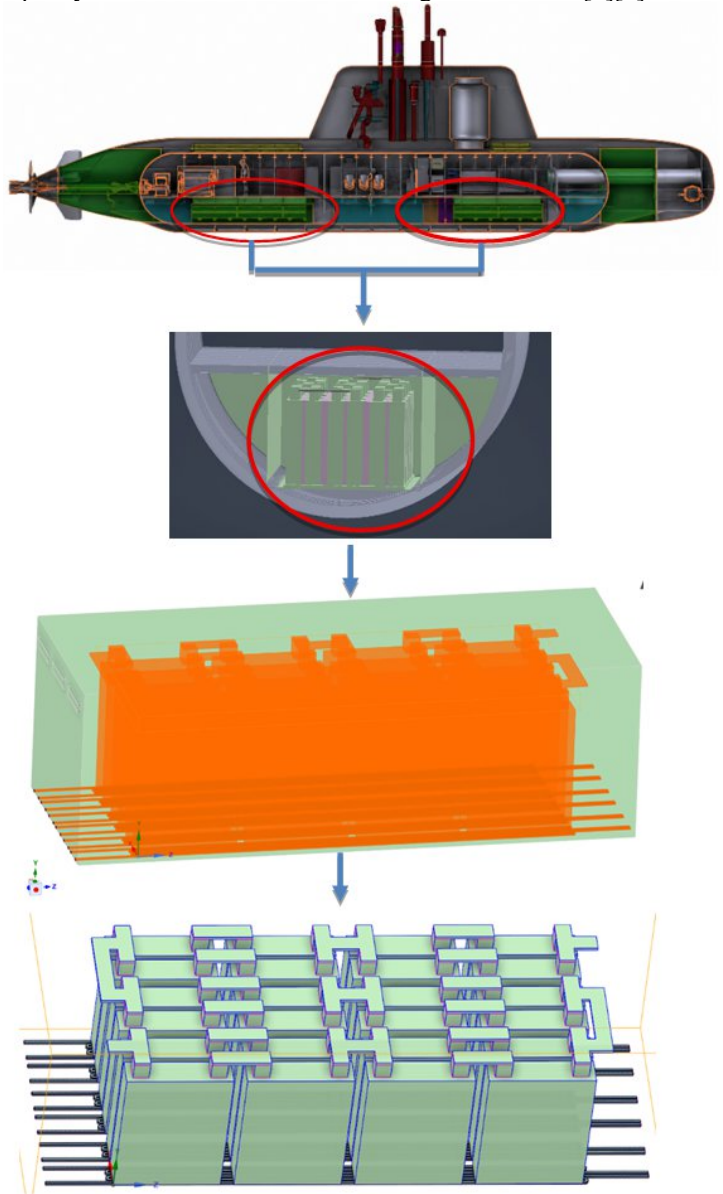

Fig. 2. Hierarchical modeling of the submarine Battery Thermal Management System (BTMS)

The visualization (Fig. 2) illustrates the transition from the macro-scale submarine hull layout to the isolated fluid domain, and down to the micro-scale solid domain comprising the 15S40P battery assembly integrated with bottom cooling channels. At the module scale, the system consists of six battery packs connected in series. Each pack contains four modules arranged in a 2-series and 2-parallel configuration, and each module has dimensions of 800 mm × 200 mm × 1000 mm. The main components affecting heat transfer, including connectors, current collectors, and bottom cooling channels, were included to preserve the dominant thermal pathways [12][13]. The surrounding battery-room air domain has dimensions of 4.5 m × 1.64 m × 1.376 m [9][15].

The solid regions, including the battery modules, cooling plates, and supporting structures, were separated from the fluid regions, including compartment air and liquid coolant. This separation allows conjugate heat transfer between the solid and fluid domains, so that heat conduction in the battery structures and convective heat removal in the air and coolant domains are calculated within the same CFD model [8][16].

2.2 Numerical framework and solver

The simulations were carried out in ANSYS® Fluent using a three-dimensional transient solver [8][17]. The conservation equations for mass, momentum, and energy were discretized using the finite-volume method [8]. The model was solved as a transient conjugate heat-transfer problem to predict the time-dependent temperature rise of the battery module and the time required to reach the 50 °C thermal cutoff. A steady initialization was used only to obtain a stable initial flow and thermal field before starting the transient discharge calculation. To reduce computational cost, wall details that were not expected to strongly affect the main airflow path around the battery modules were strongly removed from the compartment geometry.

The air flow inside the compartment was modeled using the k-ω turbulence model. This model was selected because the hybrid-cooling case includes cooling jets and recirculating airflow near the battery module surfaces, where near-wall velocity and thermal gradients are important. To keep both cooling cases comparable, the same turbulence setting was also used for the natural-convection baseline. This case is therefore treated as a passive-cooling reference with weak air motion, not as a detailed buoyancy-driven ventilation analysis. Earlier CFD studies of battery rooms and mechanically ventilated enclosed spaces have used similar simulations to examine how inlet and outlet positions, and air-change rate, influence airflow distribution [9][10]. A separate comparison of laminar, k-ε, k-ω, and buoyancy-specific turbulence formulations was not included in this work and remains a point for future study.

Fig. 3 summarizes the numerical workflow from cell-level validation to compartment-scale simulation. The Equivalent Circuit Model (ECM-based) heat-source formulation was first evaluated using published 100 Ah prismatic LFP cell data [3].

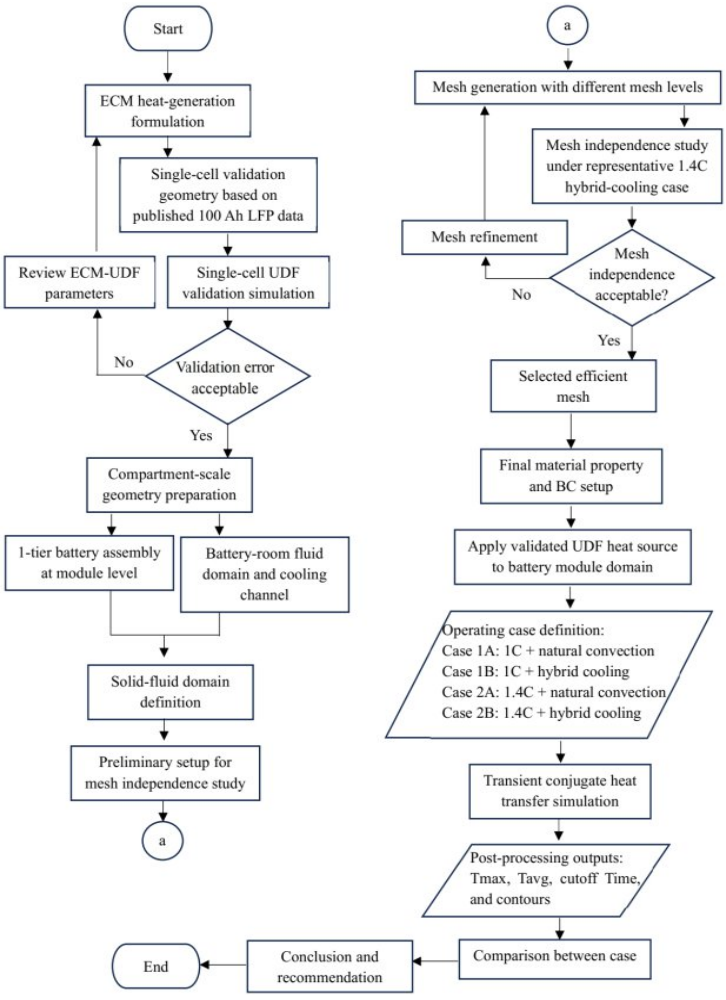

Fig. 3. CFD simulation workflow used in the present study

After validation, the same heat-source formulation was applied to the compartment-scale model comprising the battery assembly, the surrounding air domain, and the bottom cooling channels. A mesh independence check was then performed under the representative 1.4C hybrid-cooling condition. The selected mesh was used for all operating scenarios to ensure differences between cases were not due to different mesh resolutions. Finally, four simulations were evaluated: 1C natural convection, 1C hybrid cooling, 1.4C natural convection, and 1.4C hybrid cooling. The main simulation outputs were T_{max}, T_{avg}, and temperature contours, while the cutoff time was determined afterward by identifying the first time T_{max} reached the adopted 50 °C thermal threshold.

2.3 Electro-thermal model

The electro-thermal behavior of the battery cells was represented using a first-order ECM. This model estimates the transient voltage response and heat generation associated with ohmic and polarization losses[3][4]. The terminal voltage (V) is expressed as a function of the open-circuit voltage (OCV), state of charge, operating current (I), ohmic resistance (R_0), and polarization voltage (V_c) (Eq. (1)) [3].

$$V = OCV(SOC) - IR_0 - V_c \tag{1}$$

The polarization voltage is governed by the resistance-capacitance network of the first-order ECM (Eq. (2)) [3][4].

$$\frac{dV_c}{dt} = \frac{1}{C_1}\left(I - \frac{V_c}{R_1}\right) \tag{2}$$

where R_1 and $C_1$are the polarization resistance and capacitance, respectively. The internal heat generation was calculated from the electrical energy loss between the terminal voltage and the open-circuit voltage, including the ohmic and polarization contributions (Eq. (3)) [3][28].

$$Q = I(V - OCV) \tag{3}$$

2.4 UDF-based heat source formulation

To reduce the computational cost of simulating the full-tier submarine battery assembly, the heat source was implemented using a reduced-order electro-thermal formulation derived from the ECM model [3][4][13]. In this formulation, an effective resistance (R_{eff}) was used to represent the combined contribution of ohmic and polarization losses during the transient discharge process (Eq. (4)) [3].

$$R_{eff} = R_0 + \alpha R_1 \tag{4}$$

The value of α was set to 0.3 to include only part of the polarization resistance in the effective resistance term. In the reduced-order heat-source model, R0 represents immediate ohmic loss, whereas R1 is associated with the slower polarization response of the first-order ECM [3]. Because the full RC transient response was not solved directly inside the CFD domain, using the entire R1 term as an instantaneous heat source would overstate the heat release at each time step. Therefore, α was used as an empirical weighting factor for the delayed polarization contribution. With α = 0.3, the simulated temperature agreed well with the published 100 Ah prismatic LFP validation data, yielding RMSE = 0.28 °C and MAE = 0.24 °C [3]. Thus, α should be interpreted as a calibrated parameter for the present constant-current cases, not as a universal battery material property. The volumetric heat source was calculated by distributing the total heat generation over the active battery reference volume, the calculation can be obtained from Eq. (5).

$$q''' = \frac{Q_{tot}}{V_{ref}} \tag{5}$$

where V_{ref} is the reference volume of the active battery domain. During the transient simulation, SOC was updated at each time step using the Coulomb counting method (Eq. (6)) [3][4].

$$SOC(t + \Delta t) = SOC(t) - \frac{|I|\Delta t}{Q \cdot 3600} \tag{6}$$

In this formulation, SOC effects were included via the time-dependent SOC update and the SOC-dependent OCV term in the ECM. However, detailed SOC- and temperature-dependent resistance maps were not implemented in the full compartment-scale model because such data were not available for the specific commercial cell considered in this study. Therefore, SOC effects were included in a reduced-order manner through the ECM-based voltage and heat-source formulation, while the effective resistance was calibrated using the published 100 Ah prismatic LFP validation data [3][4].

2.5 Material properties

The numerical model uses density, specific heat, thermal conductivity, and dynamic viscosity for the solid and fluid regions. Because the present simulation represents a full-tier submarine battery compartment, the internal layer structure of each 100 Ah LFP cell was not resolved explicitly. Instead, the battery core was modeled as a homogenized orthotropic solid to represent the directional heat-conduction behavior of the prismatic cell stack [3][4][5]. This approach reduces computational cost while preserving the main thermal pathway of the large-format battery module.

The thermophysical properties were assigned from standard Fluent material data, published lithium-ion battery thermal modeling studies, and engineering simplifications required for compartment-scale CFD simulation [3][4][5]. Air and distilled water properties were defined near the operating temperature range, while aluminum and copper properties were assigned from standard material data. For the battery core, the lowest thermal conductivity was assigned to the through-plane direction, whereas higher in-plane values were used to represent heat spreading along the stacked layers [1][4][5]. Recent electrochemical-thermal studies of large prismatic $LiFePO_4$ cells also show that cell thickness, cooling strategy, and anisotropic heat conduction strongly affect temperature rise and temperature deviation [29].

The thermophysical properties used in the CFD simulation are summarized in Table 1. The directional effective thermal conductivity values of 0.91 / 25 / 25 W/m·K were used to represent through-plane and in-plane heat spreading in the homogenized battery module. These values should be interpreted as effective modeling parameters rather than direct measurements of the specific commercial cell used in this study.

Table 1. Thermophysical properties of the solid and fluid domains utilized in the CFD simulations

Material	ρ (kg/m³)	cp (J/kg·K)	k (W/m·K)	μ (Pa·s)
Air (25 °C)	1.184	1006	0.026	1.85×10^{-5}
Distilled water	997–998.2	4182	0.6	0.00089–0.001003
Aluminum	2700	900–903	202–237	–
Copper	8900–8960	385	387.6–400	–
Battery core	2020–2700	900–1100	0.91 / 25 / 25	–

Note: Air, water, aluminum, and copper properties were assigned from Fluent material database values and standard material data. The battery core was modeled as a homogenized orthotropic solid. The directional conductivity values of 0.91 / 25 / 25 W/m·K were used as effective parameters for through-plane and in-plane heat spreading in the compartment-scale module. The homogenized and orthotropic treatment follows the general thermal modeling approach used for prismatic and layered lithium-ion/LFP batteries [1][4][5].

2.6 Spatial discretization and mesh quality

The computational domain was discretized with an unstructured volume mesh (Fig. 4) because the battery compartment contains several irregular solid and fluid regions. Mesh refinement was applied mainly near the battery surfaces, cooling channels, and wall-adjacent fluid regions (Fig. 5). These locations were expected to have steeper velocity and temperature gradients than the bulk air region, especially around the fluid-solid interfaces where heat

transfer between the battery, air, and coolant occurs [8][11]. Before the transient calculation, the mesh quality was reviewed to avoid highly distorted cells that could reduce numerical stability or affect the heat-transfer solution [11][27].

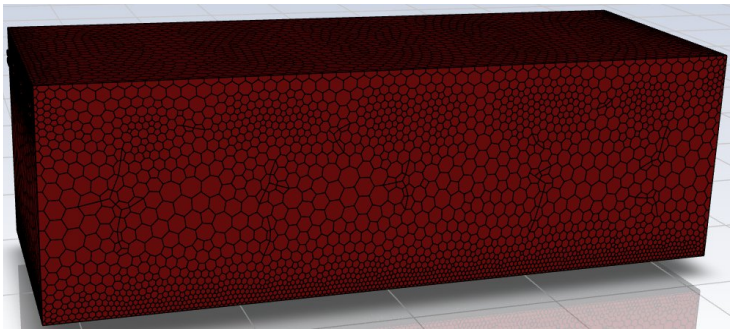

Fig. 4. Unstructured volume mesh of the submarine battery compartment fluid domain

Several mesh levels were generated during the mesh development process. Very coarse meshes were examined first, but meshes that produced nonphysical local T_{max} spikes or invalid quality indicators were not used in the final mesh-independence comparison. Therefore, five valid mesh levels were tested under the same representative 1.4C hybrid-cooling condition, with 1.5 m/s coolant velocity and 148 ACH air circulation (Table 2). The quantities compared were final T_{avg} and final T_{max}, as these parameters represent the global heat accumulation and the local maximum-temperature response of the battery module.

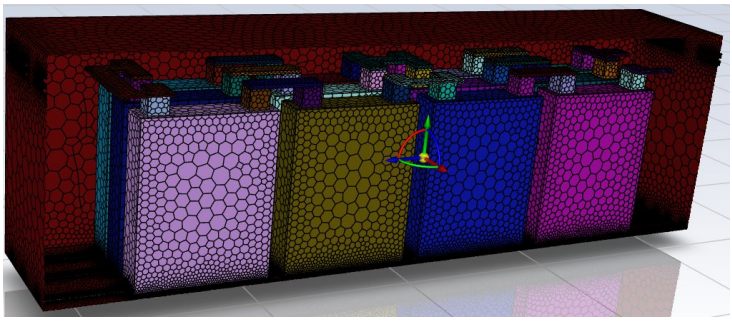

Fig. 5. Cross-sectional representation of the volume mesh, illustrating the individual LFP battery modules and cooling infrastructure embedded within the fluid domain of the compartment

Table 2. Mesh independence comparison under the representative 1.4C hybrid-cooling condition.

Elements	Min / Avg orthogonal quality	Max / Avg skewness	Final T_{avg} (°C)	Final T_{max} (°C)
1,788,922	0.074 / 0.713	0.926 / 0.271	46.039	50.699
1,930,794	0.100 / 0.723	0.899 / 0.261	46.002	50.693
2,276,679	0.110 / 0.741	0.890 / 0.243	46.019	50.798
2,956,530	0.122 / 0.772	0.878 / 0.211	46.006	50.777
3,425,634	0.104 / 0.784	0.896 / 0.200	45.766	50.639

The mesh-independence results show that the final T_{max} changes only slightly with mesh refinement. The final T_{max} values remain within 50.639–50.798 °C, while the final T_{avg} remains within 45.766–46.039 °C (Fig. 6). The coarsest valid mesh gives a final T_{max} of 50.699 °C, differing by only 0.060 °C from the very fine mesh. However, this mesh has lower minimum orthogonal quality and higher maximum skewness than the selected mesh. Therefore, the 1,930,794-element mesh was retained for the main simulations because it provides a better compromise between numerical robustness, computational cost, and thermal-response stability.

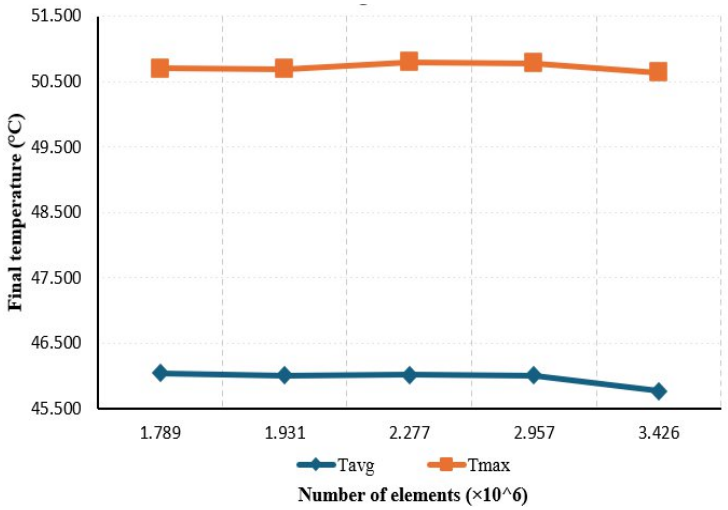

Fig. 6. Mesh independence comparison of final T_{avg} and final T_{max} under therepresentative 1.4C hybrid-cooling condition with 1.5 m/s coolant velocity and 148 ACH air circulation

Compared with the very fine mesh, the selected mesh differs by approximately 0.054 °C in final T_{max}. Although its maximum skewness is close to 0.900, the average skewness remains low at 0.261, and further mesh refinement produces only minor changes in the predicted thermal response. Additional refinement was maintained around the battery module surfaces and bottom cooling channels, as these regions control the primary heat-transfer path from the battery solid to the cooling media. Thus, the mesh was concentrated in regions that directly affect the predicted temperature field rather than being distributed uniformly across the whole room [10][11].

Table 3. Boundary conditions for each load condition (1C and 1.4C).

2.7 Operating conditions and cooling scenarios

The simulations were carried out under two constant-current discharge conditions representing high-load submarine operating profiles. The 1C discharge condition represents a standard one-hour maximum-speed submerged evasion case [6][14]. The 1.4C discharge condition represents a more severe tactical load, in which the battery supports propulsion demand, along with additional auxiliary demand during torpedo countermeasure deployment. Because the discharge current is higher, the equivalent high-load endurance decreases to approximately 2571 s. This case was used to evaluate whether the cooling system can delay the onset of thermal protection under intensified load.

For each discharge rate, two cooling conditions were evaluated. Case 1 represents the natural-convection baseline, where the coolant velocity and air circulation rate were set to 0 m/s and 0 ACH, respectively. Heat removal therefore depends on passive heat transfer between the battery surfaces and the surrounding compartment air. Case 2 represents the hybrid-cooling configuration, where liquid cooling was applied through the bottom cooling channels at 1.5 m/s and forced air circulation was applied to the compartment at 148 ACH. The liquid-cooling path removes heat from the module's lower boundary, while air circulation assists heat removal from the upper and surrounding regions. The initial and boundary conditions for both cases are summarized in Table 3.

The convection coefficient was not entered as a constant boundary value. Heat transfer from the battery surfaces to the surrounding air and coolant was instead obtained from the conjugate heat-transfer calculation. As the local velocity and temperature fields changed, the effective local heat-transfer coefficient also changed. The compartment wall was defined as a no-slip adiabatic wall, and heat transfer between the battery solids, air region, and coolant region was modeled through coupled wall interfaces.

Boundary/domain	Natural convection case	Hybrid cooling case
Discharge rate	Constant 1C or 1.4C	Constant 1C or 1.4C
Initial battery temperature	26.85°C	26.85°C
Initial volume battery room air temperature	26.85°C	26.85°C
Coolant inlet velocity	0 m/s	1.5 m/s (submarine specification)
Coolant inlet temperature	inactive	25°C(submarine specification)
Air circulation	0 ACH	148 ACH (submarine specification)
Air inlet temperature	No forced inlet	20°C (submarine specification)
Outlet condition	Pressure outlet	Pressure outlet
Compartment wall	No-slip, adiabatic wall	No-slip, adiabatic wall
Fluid–solid interfaces	Coupled wall / conjugate heat transfer	Coupled wall / conjugate heat transfer
Heat source	UDF-based volumetric heat generation	UDF-based volumetric heat generation
Radiation	Neglected	Neglected

2.8 Validation procedure

The electro-thermal model was validated by comparing the simulated transient temperature response with published experimental data for a 100 Ah prismatic LFP cell tested at an ambient temperature of 0 °C [3]. The agreement between the simulation and reference data was evaluated using the Root Mean Square Error (RMSE) and Mean Absolute Error (MAE) [13]. The validation produced an RMSE of 0.28 °C and an MAE of 0.24 °C, supporting the use of the heat-generation formulation for the subsequent module-scale simulations [3].

This validation only checks the electro-thermal heat-generation response of one 100 Ah prismatic LFP cell. It does not verify the full compartment airflow pattern, coolant distribution, or module-scale temperature gradient because experimental data for the submarine battery compartment were not available. For this reason, the validation is used to check whether the UDF heat-source formulation can follow the transient temperature trend of the reference LFP cell. The compartment-scale results are therefore treated as CFD predictions based on the assumptions and boundary conditions stated in this paper. The mesh-independence study in Section 2.6 was also used as a numerical check for the compartment model.

2.9 Modeling assumptions and limitations

Several assumptions were required to keep the compartment-scale transient CFD model practical to solve and reproducible. The battery modules were represented as homogenized orthotropic solids rather than being resolved at the individual-cell layer level. The directional thermal conductivity of the battery core was treated as an effective parameter for through-plane and in-plane heat spreading [3][4][5]. The volumetric heat source was calculated using the ECM-based UDF formulation with the empirical polarization weighting factor described earlier [2][3]. SOC was updated by Coulomb counting and linked to the SOC-dependent OCV term, but detailed SOC- and temperature-dependent resistance maps were not included because such data were not available for the specific cell considered in this study [3][4].

The operating cases were simplified as constant-current 1C and 1.4C discharges rather than pulse-load mission profiles. Air and coolant properties were also kept constant over the simulated temperature range. The same k-ω turbulence model was used for both cooling cases to keep the comparison consistent. Because air motion in the natural-convection case was much weaker than in the forced-air case, the natural-convection result should be interpreted as a passive-cooling baseline rather than a detailed buoyancy-driven ventilation analysis [9][10].

Radiation was neglected because the dominant heat-transfer paths in this model are conduction through the solid regions and convection through the compartment air and coolant [8][11][12]. The boundary conditions followed Table 3, including no-slip adiabatic walls, pressure outlets, and coupled fluid–solid interfaces for conjugate heat transfer [8][9][10]. Small wall details that were unlikely to affect the main airflow path around the modules were removed from the geometry. These assumptions should be considered when interpreting the predicted cutoff time and temperature contours.

3 Results and discussion

All reported temperature values in the results and discussion section are rounded to two decimal places unless otherwise stated.

3.1 Model validation

The validation results in Table 4 show good agreement between the ECM-UDF prediction and the reference 100 Ah prismatic LFP cell data. The RMSE and MAE are 0.28 °C and 0.24 °C, respectively, while the maximum deviation of 0.98 °C appears mainly during the initial transient phase (Fig. 7). After this early period, the relative deviation remains below 5%. These results support the use of the heat-source formulation in the compartment-scale simulations, within the validation limitations described in Section 2.8 [3][13].

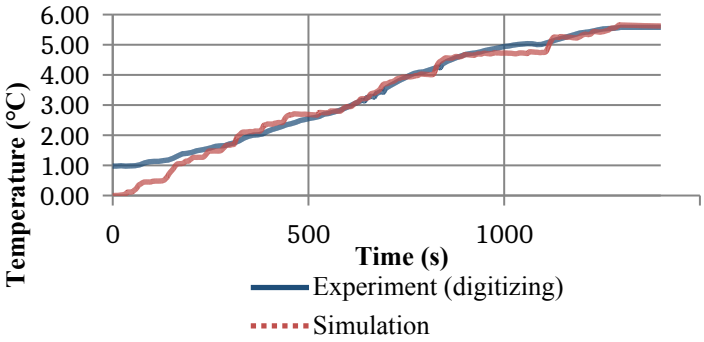

Fig. 7. Transient temperature comparison between the numerical result and the digitized experimental data for the 100 Ah LFP cell validation

Table 4. Error parameters used for the model-validation check.

Statistical Parameter	Value	Acceptance Criteria
RMSE	0.28 °C	Excellent (< 1.0 °C)
MAE	0.24 °C	Excellent (< 1.0 °C)
Maximum Deviation (Experiment vs. Simulation)	0.98 °C	Acceptable (Occurs in the initial phase)
Relative Deviation	< 5%	Valid [3]

3.2 Thermal response under 1C one-hour run

The transient T_{max} and T_{avg} responses under the 1C discharge condition are shown in Figs. 8 and 9, respectively. Under natural convection, the battery module temperature increases continuously because heat removal depends only on passive heat transfer to the surrounding compartment air. With hybrid cooling, the temperature rise is slower because heat is removed simultaneously through the bottom liquid-cooling channels and forced-air circulation in the battery room.

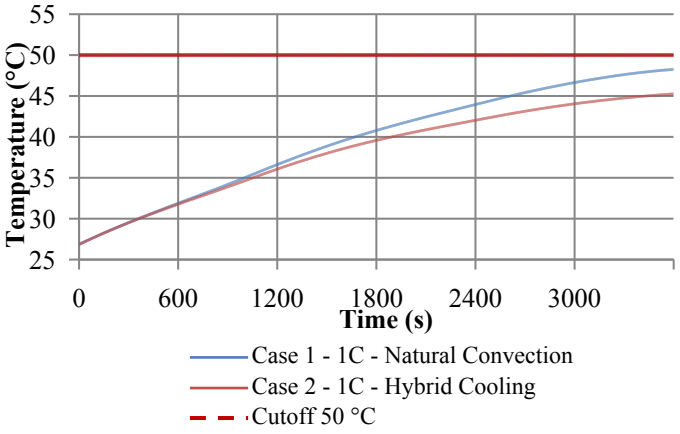

Fig. 8. Transient T_{max} comparison at 1C, with the 50°C cutoff temperature indicated by the dashed red line

At the end of the 1C simulation, hybrid cooling reduces the final T_{max} from 48.25 °C to 45.26 °C. The thermal margin to the 50 °C cutoff therefore increases from 1.75 °C under natural convection to 4.74 °C under hybrid cooling. The final T_{avg} also decreases from 47.64 °C to 40.84 °C (Table 5). These results show that hybrid cooling is effective under the 1C condition because T_{max} remains below the adopted 50 °C thermal cutoff limit while T_{avg} is also reduced.

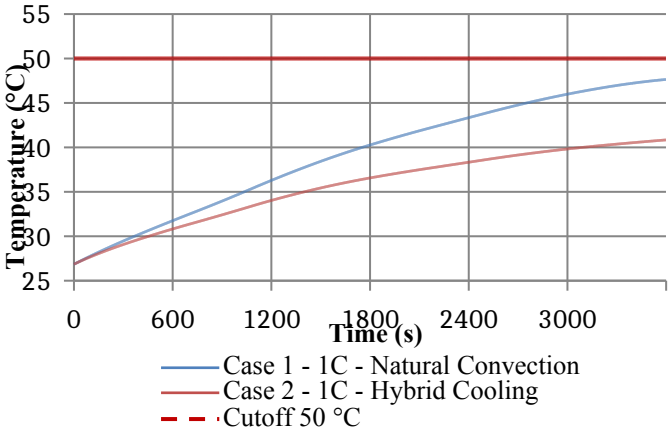

Fig. 9. Transient T_{avg} comparison at 1C, with the 50 °C cutoff temperature indicated by the dashed red line

Table 5. Comparison of thermal performance between natural convection and hybrid cooling under the 1C one-hour run condition.

Parameter	Natural convection	Hybrid cooling	Cooling effect
Maximum temperature (T_{max})	48.25 °C	45.26 °C	2.99 °C reduction
Thermal margin to 50 °C cutoff	1.75 °C	4.74 °C	2.99 °C increase
Average temperature (T_{avg})	47.64 °C	40.84 °C	6.80 °C reduction
Cutoff occurrence	Not reached	Not reached	Both cases remain below the cutoff
Operational implication	Limited thermal margin during a one-hour run	Improved thermal margin during a one-hour run	Hybrid cooling provides a safer operating window

The larger reduction in T_{avg} compared with T_{max} indicates that hybrid cooling mainly reduces global heat accumulation in the module. However, the remaining T_{max} is still governed by the local hotspot inside the large-format battery structure, where heat must be conducted from the inner region toward the cooled boundaries.

The temperature contours (Fig. 10) support this trend. Under natural convection, the high-temperature region occupies a larger portion of the module volume. In contrast, hybrid cooling creates lower-temperature regions near the upper airflow path and the bottom liquid-cooling interface. However, a warmer region remains inside the module core, indicating that internal heat conduction still limits heat removal from the central region.

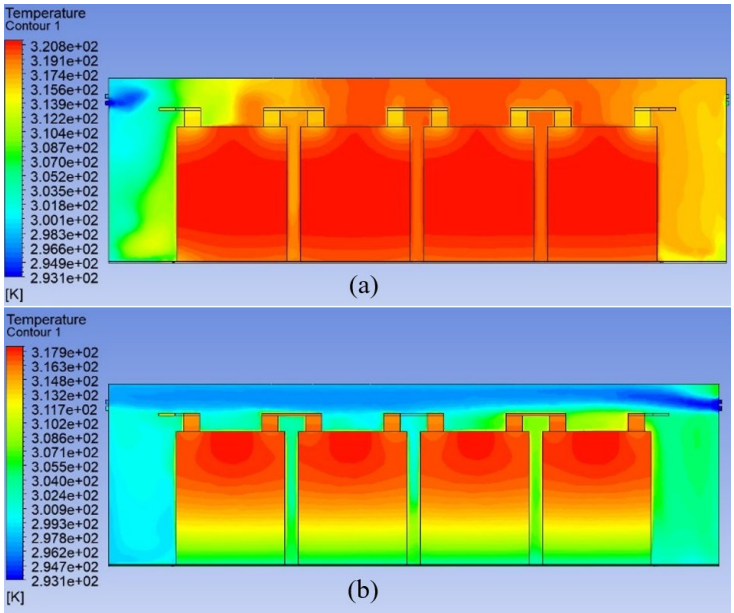

Fig. 10. Temperature contour comparison under the 1C one-hour run condition: (a) natural convection and (b) hybrid cooling

3.3 Thermal response under 1.4C intensified load

Under the 1.4C operating condition, the battery module receives a higher thermal load than in the standard 1C one-hour run. This condition represents an intensified maneuver in which the submarine is assumed to operate under maximum-speed evasion while also supporting torpedo countermeasure deployment. The higher current demand shortens the equivalent high-load endurance to approximately 2571 s. Since the dominant irreversible heat component is related to I^2R, increasing the discharge rate from 1C to 1.4C raises the internal volumetric heat generation inside the battery module [3][26][28]. As a result, the 1.4C case produces a more severe thermal response and gives a stricter test for the cooling configuration (Fig. 11).

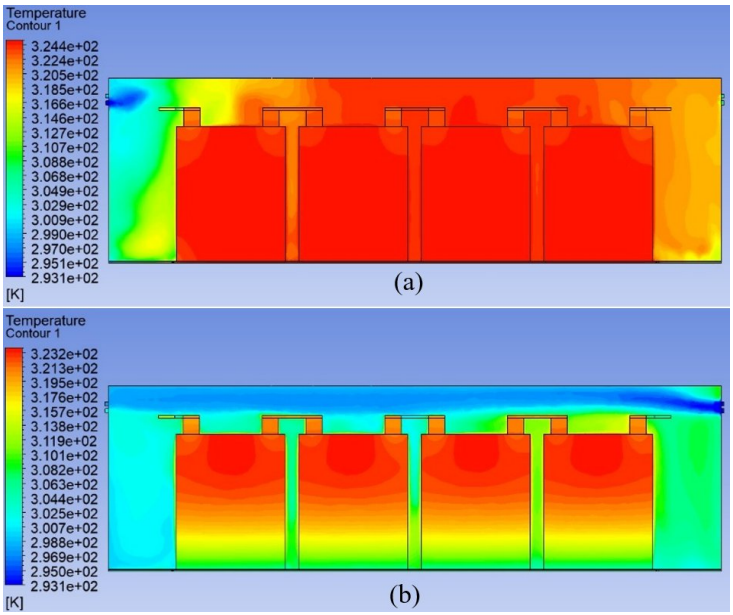

Fig. 11. Temperature contour comparison under the 1.4C intensified discharge condition: (a) natural convection and (b) hybrid cooling

The final temperature contours in Fig. 11 show that heat accumulation becomes more extensive under natural convection. The high-temperature region spreads over most of the battery module volume, indicating that passive heat removal is not sufficient for the increased heat generation at 1.4C. In the hybrid-cooling case, lower-temperature regions are formed near the upper airflow path and the bottom liquid-cooling interface. This pattern confirms that forced air circulation and liquid cooling both contribute to heat removal at the module boundaries. However, a warmer region

remains concentrated near the module core. This indicates that, at high discharge rate, the limiting factor is not only the external cooling intensity but also the internal conduction path between the heat-generating core and the cooled surfaces [12], [13].

As shown in Fig. 12, both cooling cases eventually reach the 50 °C cutoff region, but at different times. Under natural convection, T_{max} reaches 50 °C at 2140 s. With hybrid cooling, the cutoff is delayed to 2403 s. This delay of 263 s, or 4.38 min, represents a 12.3% increase in the available operating time before the thermal cutoff limit is reached.

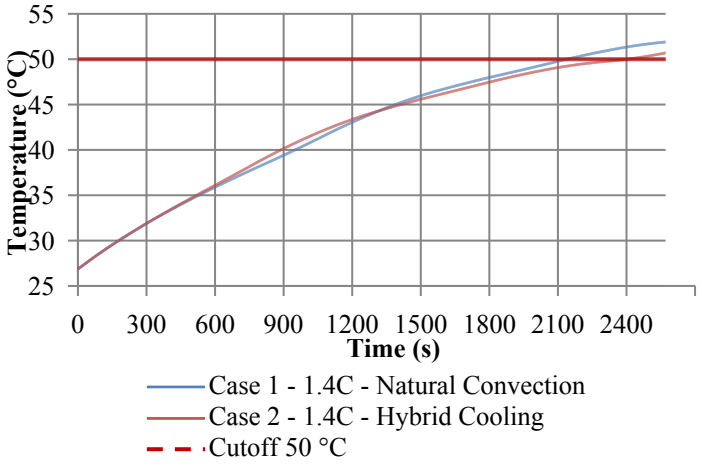

Fig. 12. Transient T_{max} comparison under the 1.4C intensified discharge condition, with the 50 °C cutoff temperature indicated by the dashed red line

A small temporary T_{max} crossover can be observed during the early-to-middle stage of the 1.4C discharge. In this interval, the hybrid-cooling case shows a slightly higher local T_{max} than the natural-convection case. However, the temperature difference in this interval is minor and should not be treated as the main thermal trend of the system. T_{max} is taken from the hottest local point in the module, so a small variation in local hotspot development may temporarily affect the curve even when the overall cooling performance is improving. The more important observation is that the hybrid-cooling case reaches the 50 °C cutoff later and produces a lower final T_{max} than the natural-convection case. At the end of the simulation, T_{max} is 51.89 °C for natural convection and 50.69 °C for hybrid cooling, corresponding to a final reduction of 1.20 °C.

The representative contours in Fig. 13 provide spatial context for the transient T_{max} curve rather than defining a separate dominant cooling mechanism from the small crossover alone. At 600 s, the temperature field is still developing, and the difference between the two cooling cases remains limited. At 1500 s, the hybrid-cooling case shows a lower overall temperature level than the natural-convection case. This supports the main trend that hybrid cooling delays the 50 °C cutoff and reduces the final T_{max}. The remaining warmer region near the module core also indicates that the local maximum temperature is still influenced by the internal conduction path between the heat-generating core and the cooled surfaces [12][13].

The T_{avg} curve (Fig. 14) gives a clearer view of the overall heat accumulation inside the module. Throughout the 1.4C discharge, T_{avg} remains lower with hybrid cooling than with natural convection. The final value decreases from 51.62 °C to 46.00 °C, or by 5.62 °C (Table 6). This reduction is larger than the reduction in T_{max}, indicating that the hybrid system removes a considerable amount of heat from the module volume, even though the hottest core region remains. In other words, the cooling system improves the average thermal condition of the battery tier, but the local hotspot remains controlled by the internal heat-spreading path.

Direct quantitative comparison with previous battery thermal management studies is not straightforward because the reported temperature reductions depend strongly on cell format, pack size, cooling geometry, inlet temperature, flow rate, discharge rate, and boundary conditions. In addition, submarine battery compartments impose stricter integration constraints than ordinary EV or surface-vessel battery systems because the available space is highly confined and the cooling system must remain compatible with compartment safety requirements.

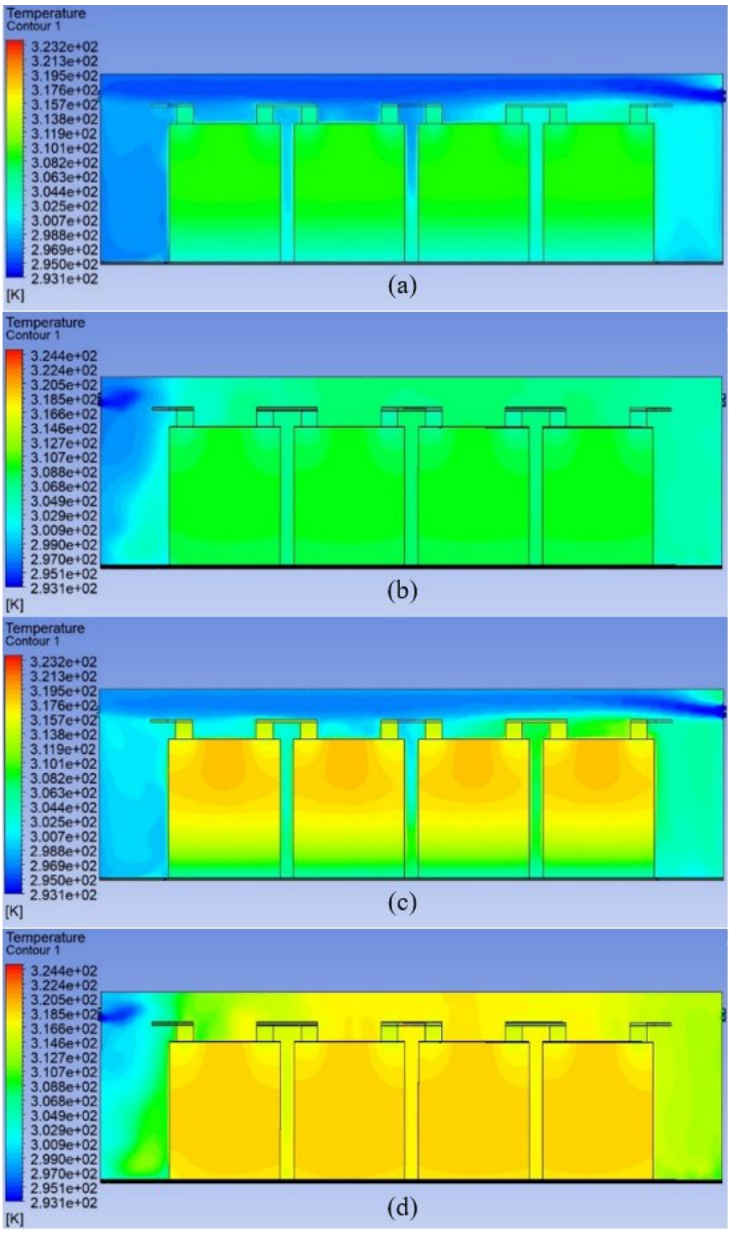

Fig. 13. Representative temperature contours around the small T_{max} crossover interval during the 1.4C intensified discharge condition: (a) hybrid cooling at 600 s, (b) natural convection at 600 s, (c) hybrid cooling at 1500 s, and (d) natural convection at 1500 s

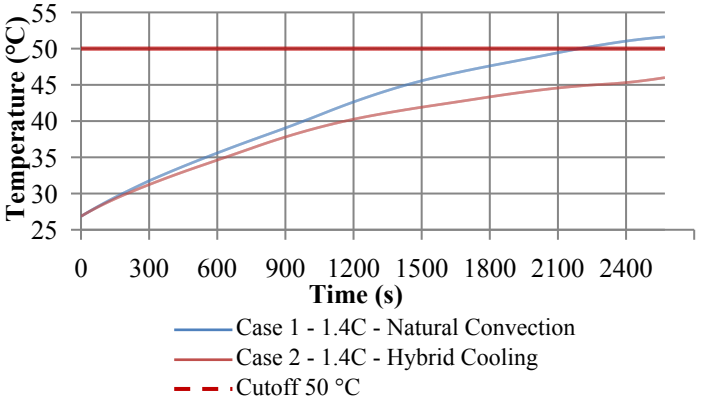

Fig. 14. Transient T_{avg} comparison under the 1.4C intensified discharge condition, confirming the continuous global cooling effectiveness of the hybrid system

Table 6. Comparison of thermal performance between natural convection and hybrid cooling under the 1.4C intensified discharge condition.

Parameter	Natural convection	Hybrid cooling	Cooling Effect
Maximum temperature (T_{max})	51.89 °C	50.69 °C	1.20 °C reduction
Average temperature (T_{avg})	51.62 °C	46.00 °C	5.62 °C reduction
Cutoff occurrence	Reached at 2140 s	Reached at 2403 s	Cutoff delayed by 263 s
Additional safe operating time	-	+ 263 s (+4.38 min)	12.30% increase before cutoff

Vessel-oriented BTMS studies have emphasized that marine battery thermal management must consider specific working conditions and operational constraints [20]. The present thermal trend is also consistent with previous $LiFePO_4$ pack, bottom liquid-cooling, and compact liquid-cooling studies, which show that cooling method, inlet temperature, flow rate, and cooling geometry strongly affect T_{max} and temperature uniformity [11][12][18]. In the present model, hybrid cooling reduces final T_{avg} by 5.62 °C under the 1.4C condition, whereas final T_{max} decreases by only 1.20 °C. This indicates that hybrid cooling is more effective in reducing global heat accumulation than in suppressing the local core hotspot, because the maximum temperature remains limited by the internal heat-spreading path of the large-format module.

3.4 Cutoff time and operational safety margin

For the 1.4C discharge case, the cutoff time provides a more useful operational indicator than the final maximum temperature alone. In a high-load submerged maneuver, a battery protection event may reduce the available propulsion power before the maneuver is completed. For this reason, the cutoff time is interpreted as the allowable duration of intensified battery operation before the adopted thermal protection limit is reached. The cutoff temperature in this study was set at 50 °C as a conservative protection threshold, considering that lithium-ion battery performance and lifetime are sensitive to elevated operating temperature [26][27].

As shown earlier in Fig. 12, the two T_{max} curves cross the 50 °C line at different times. The natural-convection case reaches the cutoff at 2140 s, while the hybrid-cooling case reaches it at 2403 s. The difference is 263 s, or about 4.38 min. Relative to natural convection, this gives 12.3% more time before the cutoff threshold is reached. Although the final T_{max} in the hybrid-cooling case remains close to the limit, the delayed crossing means the battery tier remains available for a longer period during the high-load maneuver.

The final margin gives the same tendency. At the end of the 1.4C simulation, natural convection exceeds the cutoff by 1.89 °C, while the hybrid-cooling case exceeds it by 0.69 °C (Table 7). The peak-temperature improvement is therefore about 1.20 °C. However, the additional 263 s remains useful from an operational point of view because it can provide more time for load reduction, maneuver adjustment, or countermeasure sequencing before automatic battery protection is triggered.

Table 7. Cutoff time and operational safety margin under the 1.4C intensified discharge condition.

Parameter	Natural convection	Hybrid cooling	Difference
Cutoff temperature	50 °C	50 °C	N/A
First time reaching cutoff	2140 s (35.67 min)	2403 s (40.05 min)	+263 s (+4.38 min)
Time before cutoff relative to natural convection	100% (Baseline)	112.30%	+12.30%
Final T_{max}	51.89 °C	50.69 °C	1.20 °C lower
Final margin to 50 °C cutoff	-1.89 °C	-0.69 °C	1.20 °C improvement
Operational meaning	Earlier protection activation	Delayed protection activation	Longer response window

3.5 Spatial temperature distribution and thermal bottleneck

The spatial temperature distribution gives additional information that cannot be obtained from the transient T_{max} and T_{avg} curves alone. As shown in Fig. 11, the natural-convection case produces a broader high-temperature region inside the battery module under the 1.4C intensified discharge condition. In contrast, the hybrid-cooling case shows lower temperatures near the upper airflow path and the bottom liquid-cooling interface. This confirms that the hybrid system improves heat removal at the module boundaries.

However, the contours also show that the highest temperature does not occur at the cooled surfaces, but remains inside the module core. This behavior is related to the orthotropic thermal conductivity assigned to the homogenized battery core. Heat spreads more easily in the in-plane direction than in the through-plane direction, so the heat generated in the inner region takes longer to reach the cooled upper and lower boundaries. Therefore, the main thermal bottleneck in the present configuration is not only the external cooling capacity, but also the internal conduction path between the core and the cooled surfaces [12][13].

The top-surface temperature contours in Fig. 15 provide an additional view of the lateral thermal distribution across the battery modules at the final time. Under natural convection, the warmer region is more broadly distributed over the module surface. Under hybrid cooling, the top surface shows a lower overall temperature level, indicating improved surface cooling. However, the central region remains warmer than the surrounding edges, confirming that the internal heat-spreading resistance of the large-format homogenized module still governs the remaining hotspot.

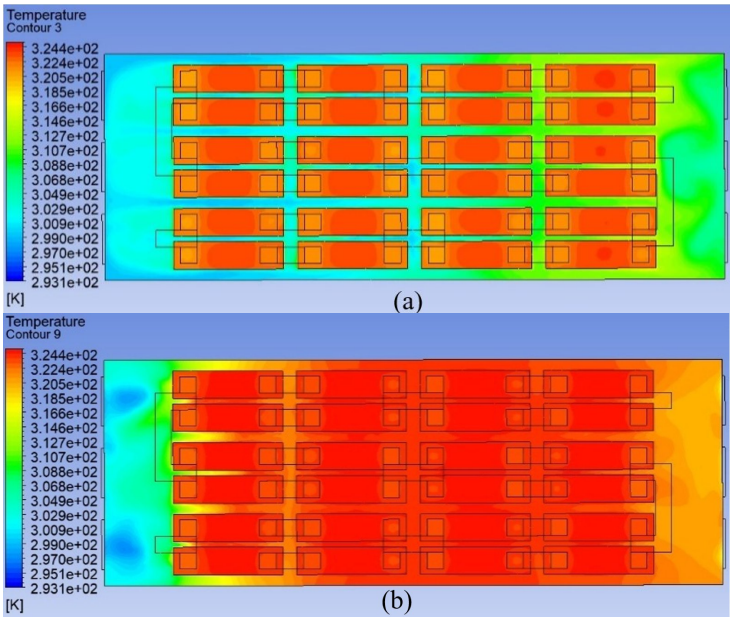

Fig. 15. Top-surface temperature contours of the battery modules at the final time under the 1.4C intensified discharge condition: (a) hybrid cooling with 1.5 m/s coolant velocity and 148 ACH air circulation, and (b) natural convection with 0 m/s coolant velocity and 0 ACH air circulation

The persistence of the core hotspot also indicates the presence of an internal thermal gradient between the heat-generating central region and the cooled outer boundaries. This interpretation is consistent with recent $LiFePO_4$ electrochemical-thermal studies showing that internal electrochemical and thermal inhomogeneity can produce non-uniform distributions of temperature, stress, and

heat-generation rate, which may accelerate degradation and affect battery safety [30]. Large-format $LiFePO_4$ cell studies also indicate that cooling boundary placement and anisotropic heat conduction can strongly influence the temperature difference between the cell core and the cooled surface [29]. Therefore, the thermal performance of the cooling system should not be evaluated solely from boundary or average temperatures, but also from its ability to reduce the internal temperature gradient between the module core and the cooled surfaces.

This spatial pattern also explains why T_{avg} decreases more than T_{max} under the 1.4C condition. Hybrid cooling reduces final T_{avg} by 5.62 °C, while final T_{max} decreases by only 1.20 °C. This difference indicates that the air and liquid cooling paths effectively reduce global heat accumulation near the upper and lower module boundaries. However, the remaining local hotspot is still controlled by internal conduction from the module core toward the cooled surfaces. Therefore, future thermal improvements should focus not only on increasing the external cooling intensity, but also on improving heat transfer from the module core to the cooled surfaces.

3.6 Operational implications for submarine maneuvering

In the 1.4C case, the time at which T_{max} first reaches 50 °C is useful for estimating the remaining response window before battery protection is expected to act. Natural convection reaches this limit at 2140 s, while hybrid cooling reaches it at 2403 s. The difference is 263 s, or 4.38 min. Although this is not a long duration, it can still matter during a high-load submerged maneuver. If battery protection reduces propulsion power during this period, the operator may have less margin for depth keeping and maneuver control. The present CFD model does not calculate submarine motion after such an event. Even so, the cutoff-time prediction estimates how long the battery can remain under intensified load before the protection threshold is reached. This response window may support earlier operational decisions, such as reducing load, adjusting maneuvering strategy, or sequencing countermeasure actions before automatic protection is triggered. This interpretation is consistent with the need to consider vessel-specific operating conditions, battery-system integration, and operational constraints in marine and submarine battery applications [6][14][20][23].

The hybrid-cooling result should also be interpreted together with its auxiliary-energy requirement. Under the 1.4C intensified load, the final T_{max} reduction is limited to 1.20 °C, while T_{avg} decreases by 5.62 °C and the cutoff time is delayed. This means that the cooling system gives a stronger benefit in reducing overall heat accumulation than in suppressing the local maximum temperature. The lower average module temperature remains useful because thermal nonuniformity and internal temperature gradients can contribute to degradation-related risks in large-format lithium-ion batteries [29], [30]. The pump and forced-air circulation system would also require auxiliary electrical power. For that reason, a full cooling-energy assessment cannot be made solely from the current CFD results. A numerical Energy Efficiency Ratio (EER) is not reported here because the model does not include pump curves, fan curves, pressure-drop-based auxiliary power, or the electrical efficiency of the cooling equipment. Some platform-specific cooling details are also not disclosed for operational confidentiality. The comparison is therefore limited to thermal effectiveness and operational margin, not to the total energy cost of running the cooling system.

Thermal-risk management remains important for marine Li-ion battery systems. Reported marine battery incidents may involve fire, explosion, toxic gas release, water ingress, coolant leakage, or failure of the battery space when the mitigation barriers are not sufficient[22]. In this paper, the 50 °C cutoff time is used solely as an early-warning limit for thermal operation. It is not intended to simulate thermal-runaway propagation or submarine motion. The results show that hybrid cooling can delay the protection threshold, but future work is still needed to include cooling-energy demand, auxiliary power consumption, and integrated operational safety control.

4 Conclusions

This study examined the transient thermal response of $LiFePO_4$ submarine battery modules under high-load discharge using a three-dimensional CFD model with conjugate heat transfer and a UDF-based heat-generation model. The main conclusions are as follows:

1. The developed compartment-scale model, using homogenized orthotropic battery modules, was able to predict transient thermal behavior efficiently and was validated against published experimental data with an RMSE of 0.28°C and MAE of 0.24°C.
2. Under the 1C discharge condition, hybrid cooling improved thermal performance by reducing the final maximum temperature from 48.25°C to 45.26°C and lowering the average temperature from 47.64°C to 40.84°C. Both cases remained below the 50°C thermal cutoff.
3. Under the 1.4C discharge condition, natural convection reached the thermal cutoff at 2140 s, while hybrid cooling delayed it to 2403 s, extending the available operating time by 263 s (12.3%).
4. The results indicate that hybrid cooling is more effective in reducing global heat accumulation than eliminating local core hotspots, which remain governed by internal conduction paths. Further work should refine thermal conductivity assumptions, optimize cooling channel layout, and validate the model with compartment-scale experimental data..

Acknowledgments

The authors thank the Indonesia Endowment Fund for Education (LPDP), Ministry of Finance of the Republic of Indonesia, for supporting this research through the LPDP scholarship program, Registration Number 202407110105391.

The authors also acknowledge the Department of Mechanical Engineering, Institut Teknologi Sepuluh Nopember (ITS), Surabaya, for providing access to the academic facilities and research environment used during this work.

Reference

[1] S. Sarkar, Md. T. Amin, M. M. El-Halwagi, and F. Khan, "Thermal behavior of LiFePO4 battery at faster C-rates and lower ambient temperatures," *Process Safety and Environmental Protection*, vol. 186, pp. 118–133, Jun. 2024, doi: 10.1016/j.psep.2024.03.095.

[2] P. Jindal, R. Katiyar, and J. Bhattacharya, "Evaluation of accuracy for Bernardi equation in estimating heat generation rate for continuous and pulse-discharge protocols in LFP and NMC based Li-ion batteries," *Applied Thermal Engineering*, vol. 201, p. 117794, Jan. 2022, doi: 10.1016/j.applthermaleng.2021.117794.

[3] A. Broatch, P. Olmeda, X. Margot, and L. Agizza, "A physical-based electro-thermal model for a prismatic lfp lithium-ion cell thermal analysis," *Energies*, vol. 18, no. 5, p. 1281, Mar. 2025, doi: 10.3390/en18051281.

[4] L. Magri, L. Sequino, and C. Ferrari, "Simulating the electrochemical-thermal behavior of a prismatic lithium-ion battery on the market under various discharge cycles," *Batteries*, vol. 9, no. 8, p. 397, Jul. 2023, doi: 10.3390/batteries9080397.

[5] H. Yu, J. Cai, and X. Zhang, "Thermal behavior simulation of lithium iron phosphate energy storage battery," *J. Electrochem. Sci. Technol*, vol. 15, no. 4, pp. 521–529, Nov. 2024, doi: 10.33961/jecst.2024.00339.

[6] F. Wang and J. Gao, "Feasibility analysis of new energy batteries equipped on conventional submarines," in *2022 7th International Conference on Integrated Circuits and*

Microsystems (ICICM), Xi'an, China: IEEE, Oct. 2022, pp. 106–109. doi: 10.1109/ICICM56102.2022.10011306.

[7] A. Gharehghani *et al.*, "Progress in battery thermal management systems technologies for electric vehicles," *Renewable and Sustainable Energy Reviews*, vol. 202, p. 114654, Sep. 2024, doi: 10.1016/j.rser.2024.114654.

[8] X. Hu, H. Xu, C. Ding, Y. Tian, and K. Yang, "Numerical study on the thermal behavior of lithium-ion batteries based on an electrochemical–thermal coupling model," *Batteries*, vol. 11, no. 7, p. 280, Jul. 2025, doi: 10.3390/batteries11070280.

[9] M. A. ElNakeeb, A. ElDegwy, and E. E. Khalil, "Numerical investigation of ventilation methods in air conditioned battery storage room," in *15th International Energy Conversion Engineering Conference*, Atlanta, GA: American Institute of Aeronautics and Astronautics, Jul. 2017. doi: 10.2514/6.2017-4718.

[10] D. D. Kim, H. Kim, W. S. Yim, and T. Lim, "An Analysis of the ventilation efficiency of various configurations of inlet and outlet vents in a residential building by CFD simulation," *Buildings*, vol. 14, no. 11, p. 3449, Oct. 2024, doi: 10.3390/buildings14113449.

[11] Y. Li *et al.*, "Numerical simulations for indirect and direct cooling of 54 V LiFePO4 battery pack," *Energies*, vol. 15, no. 13, p. 4581, Jun. 2022, doi: 10.3390/en15134581.

[12] R. Ren, Y. Zhao, Y. Diao, and L. Liang, "Experimental study on the bottom liquid cooling thermal management system for lithium-ion battery based on multichannel flat tube," *Applied Thermal Engineering*, vol. 219, p. 119636, Jan. 2023, doi: 10.1016/j.applthermaleng.2022.119636.

[13] M. Mastali *et al.*, "Electrochemical-thermal modeling and experimental validation of commercial graphite/LiFePO 4 pouch lithium-ion batteries," *International Journal of Thermal Sciences*, vol. 129, pp. 218–230, Jul. 2018, doi: 10.1016/j.ijthermalsci.2018.03.004.

[14] V. Romanovsky, B. Nikiforov, and A. Avramenko, "Improvement of lithium-ion rechargeable battery (LIRB) for Electric Ships," *J. Phys.: Conf. Ser.*, vol. 2131, no. 4, p. 042100, Dec. 2021, doi: 10.1088/1742-6596/2131/4/042100.

[15] Y. Chen, "Research on energy-saving conventional submarine air-conditioning system based on heat and humidity load calculation," *HSET*, vol. 56, pp. 407–414, Jul. 2023, doi: 10.54097/hset.v56i.10703.

[16] C. X. He, Q. L. Yue, S. B. Wan, Z. X. Guo, J. Sun, and T. S. Zhao, "Experimental and numerical investigations of liquid cooling plates for pouch lithium-ion batteries considering non-uniform heat generation," *Applied Thermal Engineering*, vol. 258, p. 124777, Jan. 2025, doi: 10.1016/j.applthermaleng.2024.124777.

[17] Y. Deng *et al.*, "Effects of different coolants and cooling strategies on the cooling performance of the power lithium ion battery system: A review," *Applied Thermal Engineering*, vol. 142, pp. 10–29, Sep. 2018, doi: 10.1016/j.applthermaleng.2018.06.043.

[18] X. Yuan, R. Zheng, J. Yang, B. Kong, and H. Shi, "Compact thermal management for high-density lithium-ion batteries: Liquid cooling solutions," *Journal of Energy Storage*, vol. 113, p. 115523, Mar. 2025, doi: 10.1016/j.est.2025.115523.

[19] S. Wankhede, A. D. Pingale, and A. Kale, "Experimental investigation on thermal management of lithium-ion battery pack for formula student electric vehicle using air-cooling system," *Energy Storage and Saving*, vol. 4, no. 1, pp. 38–47, Mar. 2025, doi: 10.1016/j.enss.2024.11.008.

[20] Y. Wu, B. Yang, X. Zhang, and S. Ying, "Research progress in battery thermal management system under vessel working conditions," *Journal of Energy Storage*, vol. 96, p. 112761, Aug. 2024, doi: 10.1016/j.est.2024.112761.

[21] M. Turhan, "Innovative IGBT-based charging systems for improved submarine battery management," *Engineering Science and Technology, an International Journal*, vol. 58, p. 101825, Oct. 2024, doi: 10.1016/j.jestch.2024.101825.

[22] P. Bugryniec, S. Khanna, M. Wootton, D. Williams, and S. Brown, "Assessment of the Risks Posed by Thermal Runaway within Marine Li-Ion Battery Energy Storage Systems - Considering Past Incidents, Current Guidelines and Future Mitigation Measures," 2024, *SSRN*. doi: 10.2139/ssrn.5052235.

[23] S. Kazemian, T. Geury, and O. Hegazy, "A review of battery systems and power electronics interfaces in electrified maritime transportation: Topologies, control techniques and future trends," *Energy Reports*, vol. 15, p. 109396, Jun. 2026, doi: 10.1016/j.egyr.2026.109396.

[24] J. Zhu *et al.*, "Simulation analysis and optimization of containerized energy storage battery thermal management system," *Journal of Energy Storage*, vol. 97, p. 112870, Sep. 2024, doi: 10.1016/j.est.2024.112870.

[25] P. Kabirzadeh *et al.*, "Integrating heat transfer and control optimization: A comprehensive review of battery thermal management systems," *Journal of Energy Storage*, vol. 131, p. 117289, Sep. 2025, doi: 10.1016/j.est.2025.117289.

[26] L. Sheng *et al.*, "Experimental and numerical approach for analyzing thermal behaviors of a prismatic hard-cased lithium-ion battery," *Journal of Energy Storage*, vol. 35, p. 102313, Mar. 2021, doi: 10.1016/j.est.2021.102313.

[27] G. Sevilgen, H. Dursun, and M. Kılıç, "Experimental and numerical investigations on the thermal performance of three different cold plates designed for the electrical vehicle battery module," *Sustainability*, vol. 15, no. 19, p. 14162, Sep. 2023, doi: 10.3390/su151914162.

[28] A. Nazari and S. Farhad, "Heat generation in lithium-ion batteries with different nominal capacities and chemistries," *Applied Thermal Engineering*, vol. 125, pp. 1501–1517, Oct. 2017, doi: 10.1016/j.applthermaleng.2017.07.126.

[29] D. Lei, Y. Wang, J. Fu, X. Zhu, J. Shi, and Y. Wang, "Electrochemical-thermal analysis of large-sized lithium-ion batteries: Influence of cell thickness and cooling strategy in charging," *Energy*, vol. 307, p. 132629, Oct. 2024, doi: 10.1016/j.energy.2024.132629.

[30] J. Mi, X. Liu, D. Zhu, L. Chen, and Y. Li, "The exploration of the internal homogeneities for a LiFePO4 pouch lithium-ion battery with a 3D electrochemical-thermal coupled model," *Next Energy*, vol. 4, p. 100127, Jul. 2024, doi: 10.1016/j.nxener.2024.100127.